# "Unveiling the Electrochemical Potential of Mg-Doped Nickel Ferrite Nanoparticles for Supercapacitor Advancements"

**S.B. Sreeja Lekshmi [a,d], S.R. Gibin [b,d], V.K. Premkumar [c], Mariappan A [b,d]**

[a]Reg.No:20113082132011, Research Scholar, Department of Physics and Research Centre, Malankara Catholic College, Mariagiri, Kaliyakkavilai-629153, Tamilnadu, India.

[b]Assistant Professor, Department of Physics and Research Centre, Malankara Catholic College, Mariagiri, Kaliyakkavilai-629153, Tamil Nadu, India.

[c]Post Doctoral Fellow Laboratory of Electrochemical Energy Storage, Institute of Environmental Resources Engineering, Zhejiang University, China.

[d]Affiliated to Manonmaniam Sundaranar University, Abishekapatti-627012, Tirunelveli,Tamil Nadu, India.

**Abstract**

The field of science has shown an abundance of interest in electrochemical capacitors, namely supercapacitors. They have a large power storage capacity and short recharging times due to their lengthy cycle life. In the present study, the Mg-doped nickel ferrite $Ni_{1-x}Mg_xFe_2O_4$ (x=0.5) was prepared by the co-precipitation method. The samples were examined using different techniques for various annealing temperatures (400℃,600℃,700℃) for structural and morphological characterization. By using XRD, the structural details of the synthesized samples were elucidated. By using TG/DT analysis the optimum temperature of the samples, determining to be 700℃. As a result, additional analysis was done for the sample annealed at 700℃. SEM and HR-TEM were used to study the nanoparticle's morphology which revealed well-defined nanostructures with an agglomerated spherical morphology. From the obtained vibrational bands, the FTIR spectra illustrate the occurrence of the spinel phase. The surface area of the nanoparticles was used to record the BET technique. The elemental composition and chemical states of constituent elements were identified through XPS analysis. The electrochemical properties of the nanoparticles were assessed by CV from which a higher capacitance reading of 412 $Fg^{-1}$ at a low scan rate of 2$mVs^{-1}$ has been reached confirming which will be suitable for supercapacitor applications.

**Keywords**: Spherical morphology, supercapacitor, surface area, spinel phase, elemental composition, optimum temperature

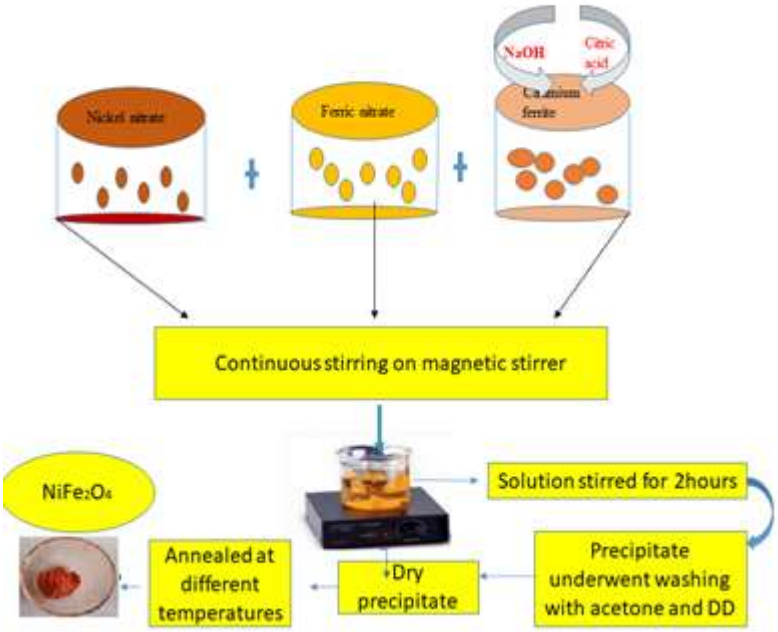


**Corresponding author at:**
Dr. S.R. Gibin
Department of Physics and Research Centre, Malankara Catholic College, Mariagiri, Kaliyakkavilai-629153, Tamilnadu, India.
E-mail:gibin.physics@gmail.com

## 1.INTRODUCTION

The demand for innovative energy generation and storage technologies has increased due to the growing need for clean and renewable energy sources as well as the non-renewable nature of fossil fuels and their decreasing availability [1]. Researchers have dedicated significant efforts to studying supercapacitors due to their numerous advantages. One notable benefit is their ability to quickly store and release energy, making them well-suited for applications requiring rapid power delivery, like regenerative braking in electric vehicles or managing power fluctuations in renewable energy systems [2-3]. The electrode materials used in supercapacitors, often referred to as ultra-capacitors or electrochemical capacitors, have a high surface area, and the electrolytic dielectrics are thin. This unique design enables them to achieve capacitances that are several orders of magnitude greater than those of traditional capacitors [4-5]. In both electric double-layer capacitors (EDLCs) and supercapacitors, electrode materials such as transition metal oxides and highly porous activated carbon are commonly used [14].

Consequently, in recent decades, transition metal oxides and certain ferrites have emerged as preferred electrode materials for supercapacitor applications due to their ability to provide high specific capacitance. These alternative materials help overcome the limitations associated with activated carbon, thereby enhancing the performance of supercapacitors [6-8]. Low energy density refers to the limited amount of energy that can be held per unit volume or mass of the electrode material. Supercapacitors typically exhibit lower energy densities compared to batteries due to their reliance on surface adsorption or electrostatic double-layer capacitance [9-10]. $NiFe_2O_4$, known as nickel ferrite, is a ferrite material of great importance due to its specific uses in various applications. It has practical uses in things like microwave electronics, ferrofluids, color imaging, high-density magnetic storage, and MRI contrast agents. As a spinel ferrite, $NiFe_2O_4$ functions as an n-type

semiconductor. It can exhibit paramagnetic, superparamagnetic, and ferromagnetic properties, and its behavior can vary based on parameters including particle size and shape [11].

Ferrites have gained prominence across various fields owing to their impressive structural, electrical, magnetic, and chemical properties. Among the wide range of ferrites, magnesium, and nickel ferrites are particularly appealing due to their cost-effectiveness, environmentally friendly nature, substantial magneto crystalline anisotropy, and chemical stability Furthermore, these ferrites have recently exhibited remarkable electrochemical performance in supercapacitors, underscoring their significance in energy storage applications [12,13,15]. Several methods can be employed to synthesize nanoparticles, among which the co-precipitation method is a simple and cost-effective technique. In this present research work, magnesium-doped nickel ferrite was synthesized by the chemical co-precipitation method, to study the structural, morphological properties and electrochemical properties. Based on the evaluation of existing published research reports, there is a notable scarcity of studies examining the electrochemical performance of magnesium substituted with nickel ferrites. This research paper aims to fill the existing research gap by investigating the electrochemical properties of $Ni_{1-x}Mg_xFe_2O_4$, which are magnesium substituted with nickel ferrites.

## 2. EXPERIMENTAL STUDIES

A unique co-precipitation technique was used to create nanocrystalline $Ni_{1-x}Mg_xFe_2O_4$ (x=0.5) nanoparticles. The chemicals are from Merck Chemicals and are of the highest purity. For synthesizing $Ni_{1-x}Mg_xFe_2O_4$ nanoparticles $Mg(NO_3)_2.6H_2O$, $Ni(NO_3)_3.6H_2O$, $Fe(NO_3)_3.9H_2O$ and citric acid($C_6H_8O_7$) were taken as a precursor. All of the metal nitrates were weighed, and then dissolved in 20 ml of deionized water (DD), together with 0.29 M citric acid and 4 M NaOH. The metal nitrates were combined in a 1:2:3 molar ratio after the dissolution. The final step was to add 4M off NaOH solution as a precipitating agent and stir the entire solution for 750 rpm at 80℃ to reach a PH value of roughly 9. The agitated solution was then left to continue stirring continuously for three hours at 80°C. We get a dark brown precipitate after thorough stirring. To produce a clear precipitate, acetone, and deionized water are utilized for washing. The precipitate was dried by using a heating mantle for 2h at 90-100$^o$C to obtain $NiMgFe_2O_4$ powder and these samples were annealed at different temperatures such as 400$^o$C,600$^o$C,700$^o$C.

To identify the crystalline phase of the Mg-doped $NiFe_2O_4$ nanoparticles, the researchers employed the X-ray Diffraction (XRD) technique. The XRD analysis was performed using a BRUKER USA D8 Advance, Davinci device, which utilized CuKα radiation with a wavelength (λ) of 1.54060 Å. The XRD instrument operated at 40kV and 30mA. The XRD measurements were conducted by scanning the samples over a range of 2θ values from 20° to 80°. The scan speed was set at 10°min$^{-1}$. To estimate the mean crystal diameter, the Debye Scherer formulation was used.

$$D = \frac{K\lambda}{(\beta \cos\theta)}$$

Here, D stands for the average crystal diameter, K is the constant (k=0.9) associated with crystal shape, λ denotes the X-ray wavelength, β is the Full width at half-maximum FWHM of the diffraction peak, and θ is the Bragg angle.

The phase of the sample was determined using the JCPDS database, which is the Joint Committee of Powder Diffraction Standards. To evaluate the degradation performance of the prepared sample a TG/DT analysis was led using a NETZSCH-STA 449 F3 JUPITER analyzer. Elemental imaging analysis was performed using an EVO 18 model Scanning Electron Microscope (SEM) after sputtering the samples. The morphology and size of the samples were studied using HR-TEM analysis with an FEI-TECNAI G2-20 TWIN model operating at 200 kV. Elemental analysis was carried out

using EDX with a Bruker EDX instrument featuring an LN2-free detector. The material was scattered across a copper grid that was coated with carbon to produce SAED patterns. XPS measurements were performed using the ULVAC-PHI MODEL: PHI5000 Version Probe 111. FTIR analysis was conducted using a Spectrum Two model. The Brunauer-Emmett-Teller (BET) method was used by Quantachrome Instruments' Autosorb IQ series to calculate the specific surface area of the nanoparticles. Utilizing the Versa STAT MC model, cyclic voltammetry (CV) was used to examine the electrochemical characteristics of the nanoparticles.

## 3. RESULT AND DISCUSSION

### 3.1 X-ray diffraction

The structural study of Mg-doped nickel ferrite nanoparticle samples $Ni_{1-x}Mg_xFe_2O_4$ (x=0.5) was described using X-ray diffraction (XRD)analysis, followed by different annealing temperatures (400 ºC,600 ºC,700 ºC) which depicts in Fig.1.The primary peak is centered at 2θ=35.4 and corresponds to the miller indices (311) crystalline plane. The XRD peaks demonstrated only a single cubic spinel phase without showcasing any impurities, the same report was reported earlier by Bhandare *et al;* [16]. The diffraction peaks were observed as follows 32.38°, 35.54°, 36.20°, 41.22°, 56.6°, and 62.5° shows the crystal planes (200), (311), (222), (400),(422),(511),(440) respectively. The planes are in good agreement with the reference pattern from the JCPDS database (card no:74-2081 for $NiFe_2O_4$ and card no:89-4924 for $MgFe_2O_4$). With the use of the Debye-Scherrer equation, the average crystalline size of the particles was determined

$$D = \frac{K\lambda}{(\beta \cos\theta)}$$

Here, D-represents for average crystal size, K is a diffraction constant (k = 0.9) as related to crystal shape, λ denotes the wavelength of the incident X-ray, β corresponds to the Full width at half maximum (FWHM) of the characteristic peak in radius, then θ denotes the Bragg diffraction angle. The calculated crystalline size of the Mg-doped nickel ferrite was found to be around 18 nm. [17].

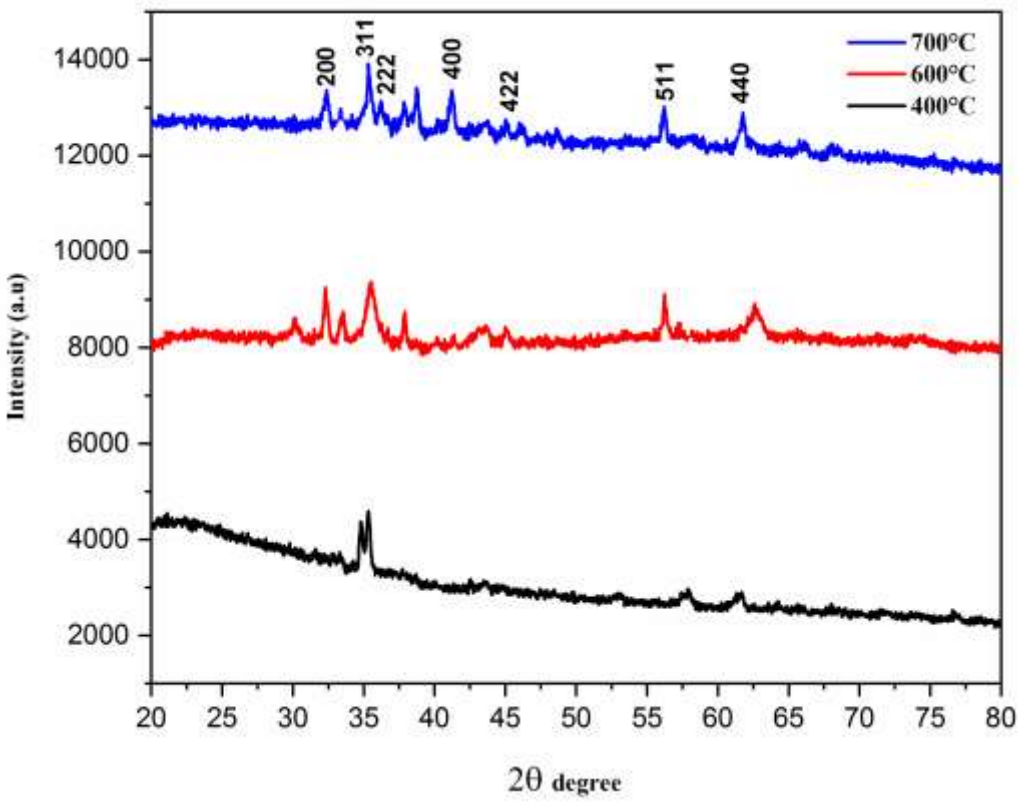


**Fig .1.** XRD images of $Ni_{1-x}Mg_xFe_2O_4$ (x=0.5) at 400℃,600℃,700℃

## 3.2 Fourier transform infrared spectroscopy

The $Ni_{1-x}Mg_xFe_2O_4$ (x=0.5) nanoparticles' FTIR spectra are shown in Fig.2. The measurements were conducted within the frequency range of 4000-400 $cm^{-1}$. The spectra exhibited prominent absorption bands at around 564 $cm^{-1}$ and 425 $cm^{-1}$, representing the principal absorption regions. The highest band ($v_1$) was observed between 515 $cm^{-1}$ and 525 $cm^{-1}$, indicating the stretching vibration of tetrahedral metal-oxygen bonds. In contrast, the lowest bands ($v_2$) appeared within the range of 409 $cm^{-1}$ to 425 $cm^{-1}$, signifying the stretching vibration of octahedral metal-oxygen bonds [18]. The spectra also displayed bands in the vicinity of 3391 $cm^{-1}$ and 1450 $cm^{-1}$, corresponding to the stretching and bending vibrations of H-O, suggestive of free or absorbed water molecules. This finding corroborates a previous report by Mund *et.al;* [19]. Furthermore, distinctive absorption bands were detected at approximately 2970 $cm^{-1}$, 1639 $cm^{-1}$, and 901 $cm^{-1}$, representing the symmetric stretching, bending, and twisting vibrations of the C-H bond, respectively [32].

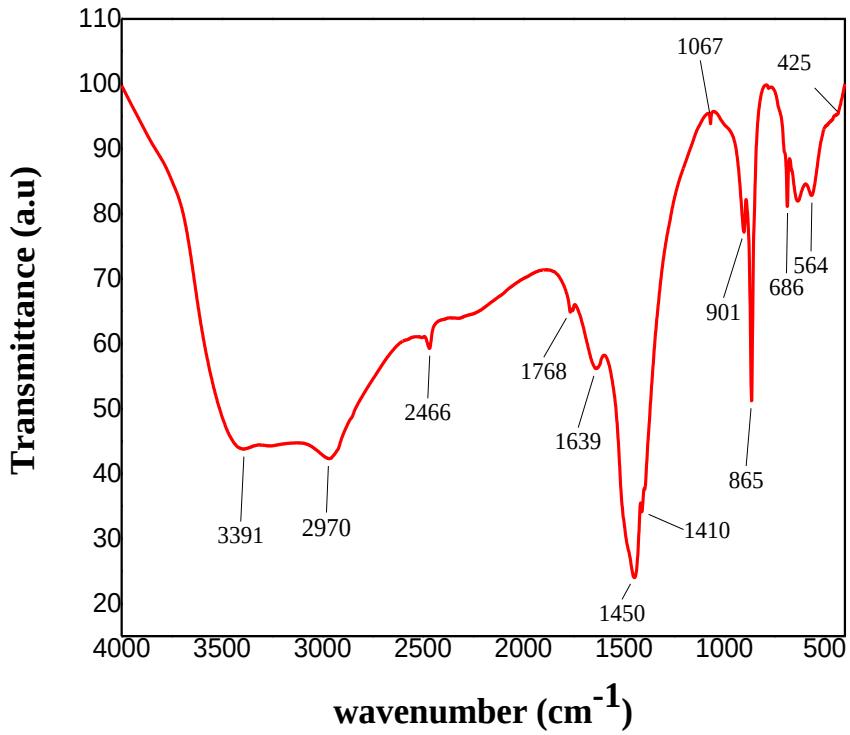


**Fig .2** FTIR spectrum of $Ni_{1-x}Mg_xFe_2O_4$ (x=0.5) at 700℃

### 3.3 Scanning Electron Microscope

A scanning electron microscope was used to study the sample's morphology. Fig.3. (a,b,c) shows the SEM images of the synthesized $Ni_{1-x}Mg_xFe_2O_4$ (x=0.5) at 700°C. These images confirm the formation of $NiMgFe_2O_4$. The particles exhibit a well-arranged and fine-grained, roughly spherical structure with only a few agglomerations. This can be associated with the strong magnetic interaction between the particles. [20,31]

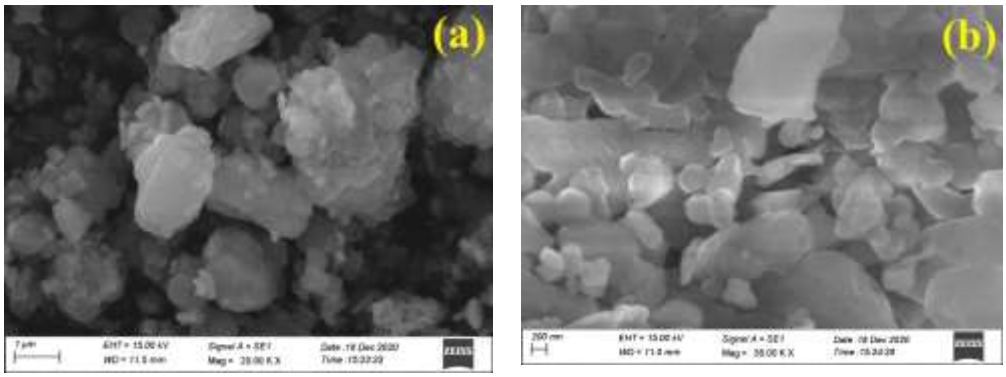

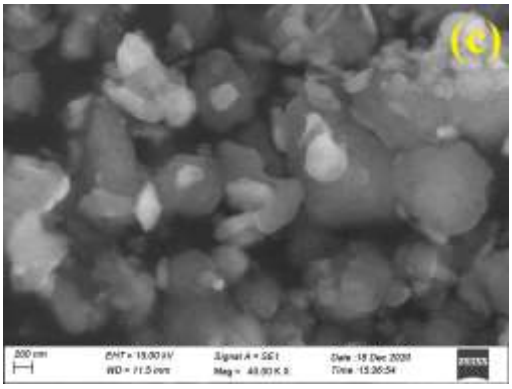


**Fig.3. (a,b,c)** SEM images of $Ni_{1-x}Mg_xFe_2O_4$ (x=0.5) at 700℃

### 3.4 Energy Dispersive X-ray Spectroscopy

EDX investigation was employed to investigate the elemental composition of the spinel $NiMgFe_2O_4$ sample. Fig.4. depicts the results of the analysis. The compositional spectrum clearly shows peaks corresponding to the components of $NiMgFe_2O_4$, confirming the presence of oxygen, nickel, magnesium, and iron. Furthermore, the spectrum indicates the absence of any additional impurities, providing further confirmation of the sample's purity.

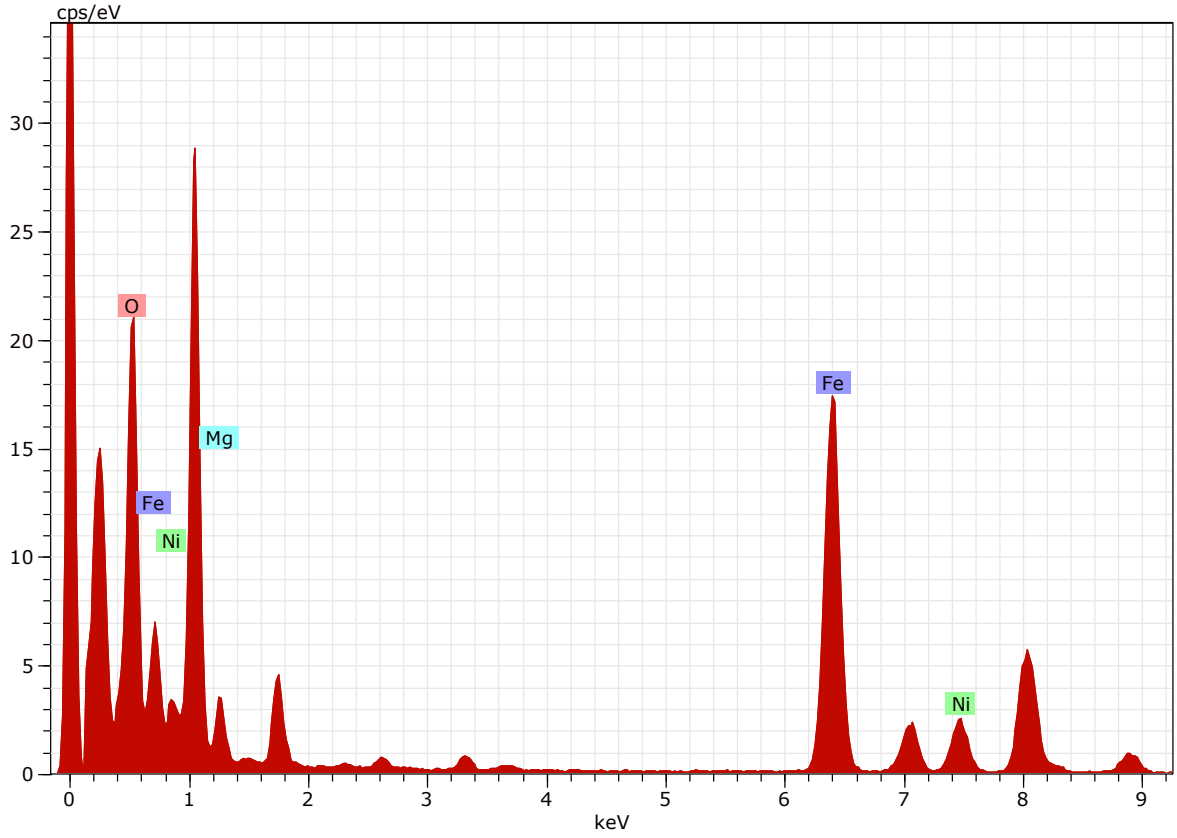


**Fig .4** EDX analysis of the sample $Ni_{1-x}Mg_xFe_2O_4$ (x=0.5) at 700℃

| **Element** | **Series** | **Net** | **unn.C [wt.%]** | **norm.C [wt.%]** | **Atom. C [at.%]** | **Error (3 Sigma)** |
|---|---|---|---|---|---|---|
| Oxygen | K-series | 27874 | 40.11 | 40.11 | 68.63 | 3.76 |

| | | | | | | |
|---|---|---|---|---|---|---|
| Nickel | K-series | 7093 | 8.15 | 8.15 | 3.80 | 0.87 |
| Iron | K-series | 46391 | 48.28 | 48.28 | 23.67 | 4.48 |
| Magnesium | K-series | 4347 | 3.46 | 3.46 | 3.90 | 0.42 |

**Table. 1** Elemental composition of $Ni_{1-x}Mg_xFe_2O_4$ (x=0.5)

### 3.5 High-resolution transmission electron microscope

In order to gain insight into the morphology of $Ni_{1-x}Mg_xFe_2O_4$ (x=0.5) nanoparticles, HR-TEM and SAED studies were conducted. Fig.5. (a,b,c,d) shows the results of these studies. The HR-TEM images reveal a nanocrystalline structure with agglomeration, which is attributed to the magnetic interaction between the nanoparticles. The synthesized samples exhibit a roughly spherical shape. By using image 'j' software, the average particle size was estimated to be 21.84 nm, as depicted in Fig.5(e) which corresponds well with the size determined by XRD (X-ray Diffraction) measurements. The SAED pattern exhibits distinct and well-separated continuous rings, indicating that the Mg-doped $NiFe_2O_4$ nanoparticles possess a well-crystalline nature [21].

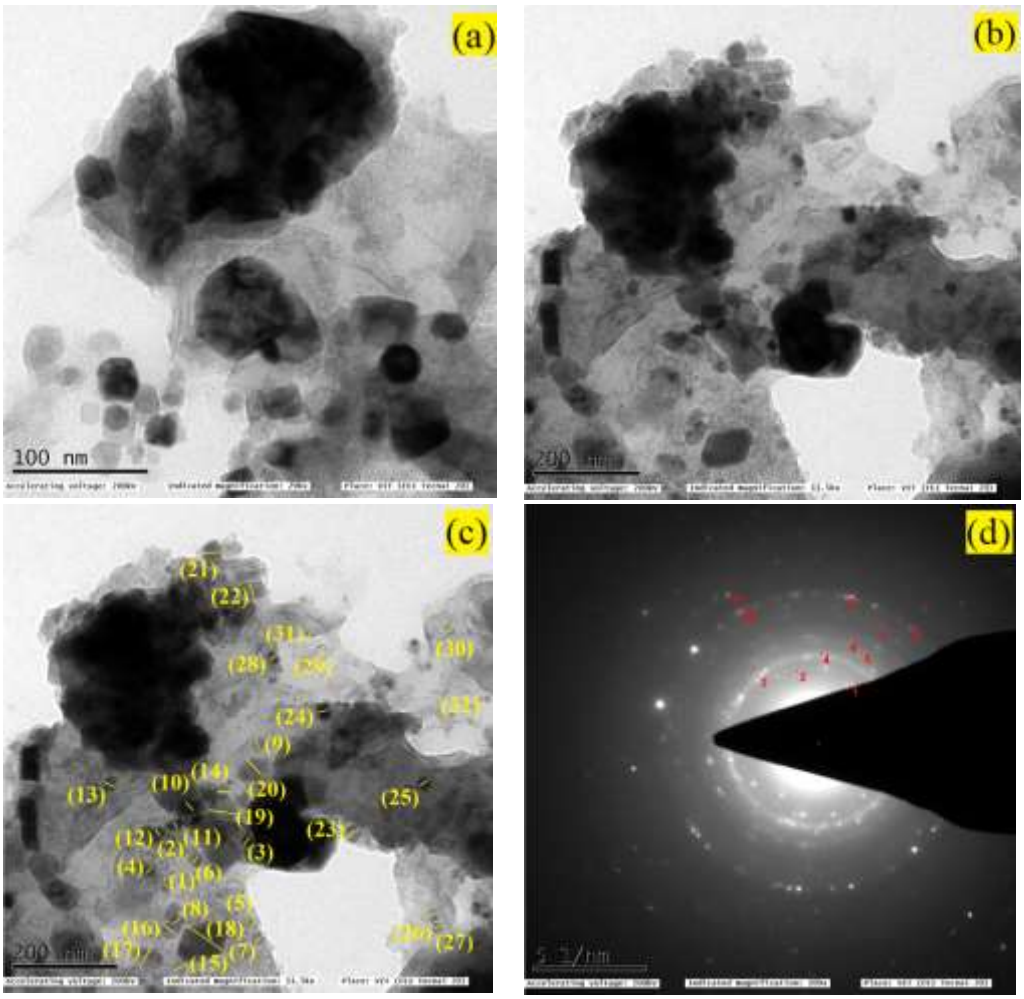


**Fig.5. (a,b,c,d)** HR-TEM images of $Ni_{1-x}Mg_xFe_2O_4$ (x=0.5) at 700℃

| No.of Particles | Particle size (nm) | No.of Particles | Particle size (nm) |
|---|---|---|---|
| 1 | 10.848 | 18 | 39.2652 |
| 2 | 11.432 | 19 | 31.352 |
| 3 | 13.458 | 20 | 25.379 |
| 4 | 14.103 | 21 | 20.036 |
| 5 | 15.713 | 22 | 19.778 |
| 6 | 15.08 | 23 | 18.686 |
| 7 | 16.204 | 24 | 17.13 |
| 8 | 17.073 | 25 | 16.852 |
| 9 | 18.079 | 26 | 15.116 |
| 10 | 18.726 | 27 | 15.944 |
| 11 | 19.956 | 28 | 14.93 |
| 12 | 23.356 | 29 | 13.742 |
| 13 | 28.513 | 30 | 12.423 |
| 14 | 34.159 | 31 | 11.398 |
| 15 | 46.935 | 32 | 10.279 |
| 17 | 40.932 | Mean | 21.844 nm |

**Table 2**. No. of particles and particle size $Ni_{1-x}Mg_xFe_2O_4$ (x=0.5) using image 'j' viewer software from HR-TEM.

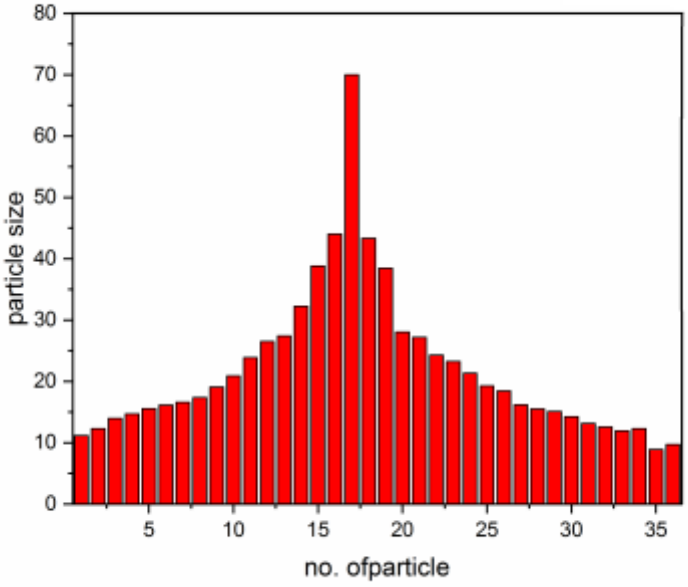


**Fig.5. (e)** Average particle size using image 'j' viewer software from HR-TEM

### 3.6 Thermo Gravimetric and Differential Thermal Analysis

The TG/DT analysis curve precursor was obtained by means of the co-precipitation method. The analysis was conducted within a temperature range of 35℃ to 800℃. It is depicted in Fig.6. During the initial decomposition step (35℃ to 243℃), a weight loss of 9% was observed, which can be attributed to the adsorption of water molecules. The second decomposition step (243℃ to 390℃) exhibited an exothermic peak at 322℃ and an endothermic peak at 379℃, indicating the decomposition of metal

nitrates and the release of $CO_2$ and $N_2$[22]. The third decomposition step (390℃ to 640℃) involved the continuous de-hydroxylation process [23]. Beyond 640℃, the weight loss was almost negligible, indicating stability and confirming the formation of $NiMgFe_2O_4$ [24].

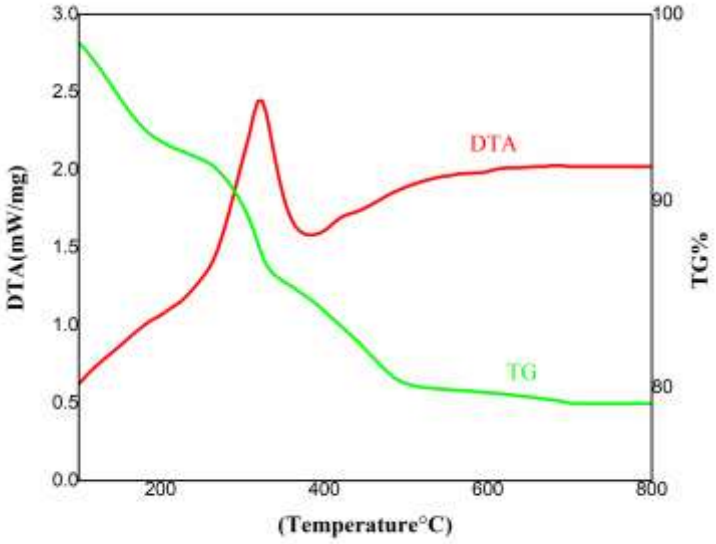


**Fig.6.** TG/DT analysis of $Ni_{1-x}Mg_xFe_2O_4$ (x=0.5) at 700℃

### 3.7 X-ray Photoelectron Spectroscopy

The XPS study is an important way to identify quantitatively determine the surface components and composites of the sample. The wide scan XPS spectra of the sample in the binding energy range(0–1400eV) are shown in Fig.7(e). The individual components of the composites were confirmed by individual XPS Spectra of Oxygen (O1s), Ferrous (Fe2p), Nickel (Ni2p), Magnesium (Mg1s) and Mg-doped $NiFe_2O_4$ as shown in Fig.(7e) respectively

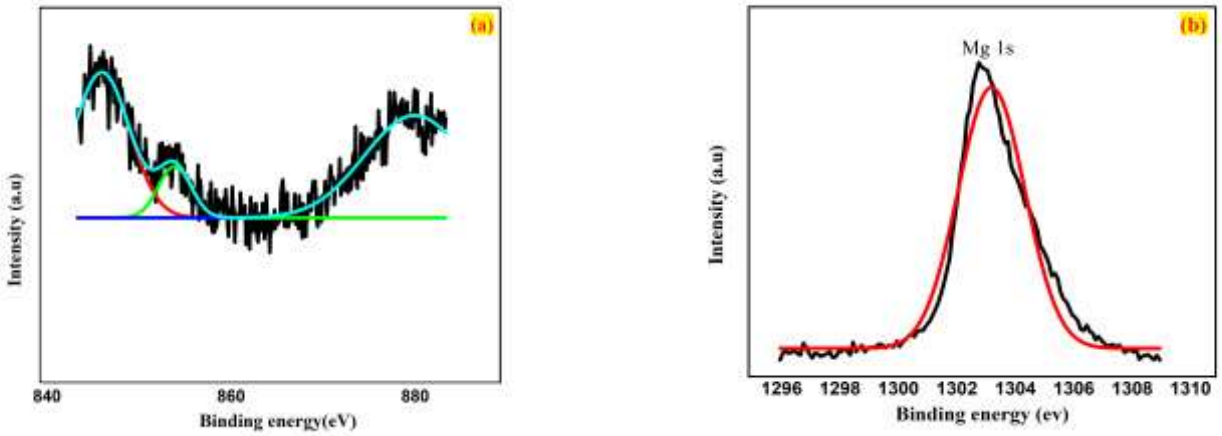

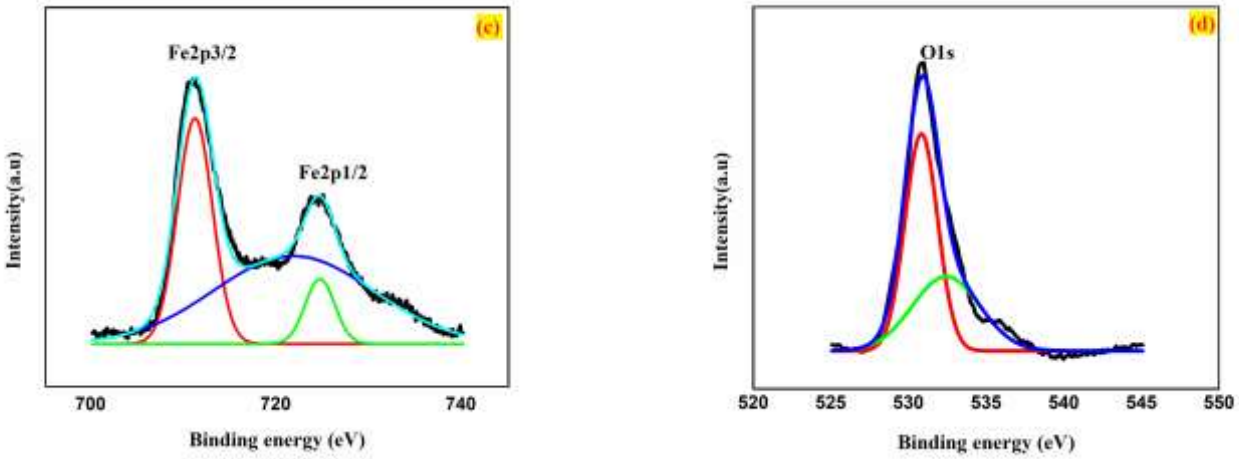


**Fig.7(a-d)** XPS spectra of Ni2p, Mg1s, Fe2p,O1s of $Ni_{0.5}Mg_{0.5}Fe_2O_4$

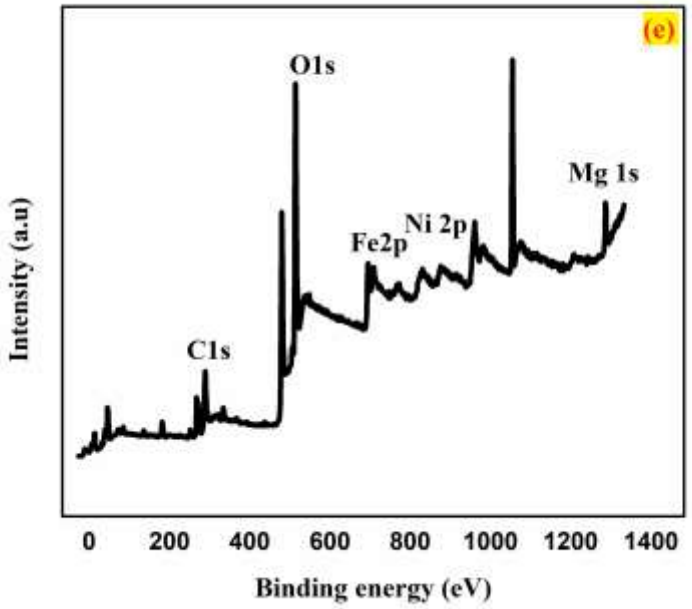


**Fig.7(e)** Wide scan XPS - spectra of Mg-doped $NiFe_2O_4$ sample.

The wide-scan XPS spectra of the sample are given in Fig.7(e) which displays the binding energies assigned to O 1s (Fig.7d), Fe2p (Fig.7c), Ni2p (Fig.7a), Mg1s (Fig.7b) and Mg-doped $NiFe_2O_4$ sample (Fig.7e) on the surface of Magnesium along with Nickel Ferrite (Mg-doped $NiFe_2O_4$ sample). The binding energies of the individual components O1s, Fe2p, Ni2p, and Mg1s were tabulated in Table.3. The binding energies of Ni2p1 and Ni 2p1/2 for the sample were obtained, respectively as 868.45 eV and 867.5 eV (Fig.7(e) and Table 3). The value of FWHM for each spin–orbit component is the same, but for Ni2p the Ni2p1/2 component is much broader than the Fe2p peak. It is caused by the Coaster – kroning effect (post–ionization) Ni 2p1/2 peak is much shorter compared to Fe2p3/2. XPS spectra of magnesium, there are two peaks in the binding energy region Mg1s and Mg1s1/2 were observed, where the peaks Mg (Mg1s) 1303.08 eV) and Mg ((Mg1s1/2)

1304.07 eV) correspond well with the values in the literature (Fig.7(e) and Table 3). XPS results also reveal and confirm the presence of $Fe^{2+}$, $Ni^{2+}$, and $Mg^{+}$ on the surface of the sample Mg doped $NiFe_2O_4$ sample [25-28].

| Name of Elements | Peak BE | FWHM eV | Area (P) CPS.eV |
|---|---|---|---|
| **O1s** | 531.49 | 3.93 | 950223.36 |
| **Mg1s** | 1304.07 | 3.43 | 152596.7 |
| **Fe2p** | 711.82 | 5.98 | 554246.24 |
| **C1s** | 285.93 | 4.64 | 209273.84 |
| **C1s** | 284.79 | 2.12 | 23924.85 |
| **O1s** | 530.93 | 2.99 | 122216.49 |
| **Fe2p** | 711.1 | 5.18 | 76335.08 |
| **Mg1s** | 1303.08 | 2.55 | 19634.1 |
| **Ni2p1** | 868.45 | 0.99 | 8231.62 |

**Table 3.** Binding Energies of O1s, C1s, Fe2p, Ni2p, Mg1s and Ni2p1 components in the synthesized sample.

### 3.8 Brunauer-Emmett Teller (BET)

Fig 8a shows the typical $N_2$ adsorption and desorption isotherms of the sample, showing that the amount of adsorbed $N_2$ increases with the increase in relative pressure and that adsorption takes a slightly different path than desorption and results in a hysteresis loop. In general, this type of isotherm with an H3 hysteresis loop is symptomatic of the material's mesoporous nature. The occurrence of capillary condensation in the mesoporous is associated with type IV isotherms that have hysteresis loops. At higher pressures, the adsorption was increased due to capillary condensation in the pores during the adsorption process and changes in the structure of the pore during the desorption process. The BET surface area for the nanocrystalline material was calculated to be 21.36 $m^2/g$. The attained pore size distribution of the $NiMgFe_2O_4$ was observed at 3.05 nm from Fig 8b. Thus, it is established that the sample is mesoporous in nature. A larger surface area would increase the number of active sites, facilitate redox reactions, and facilitate ion transfer. The outcome shows that the sample's observed porosity and surface area may be helpful in enhanced supercapacitor performance [33-34].

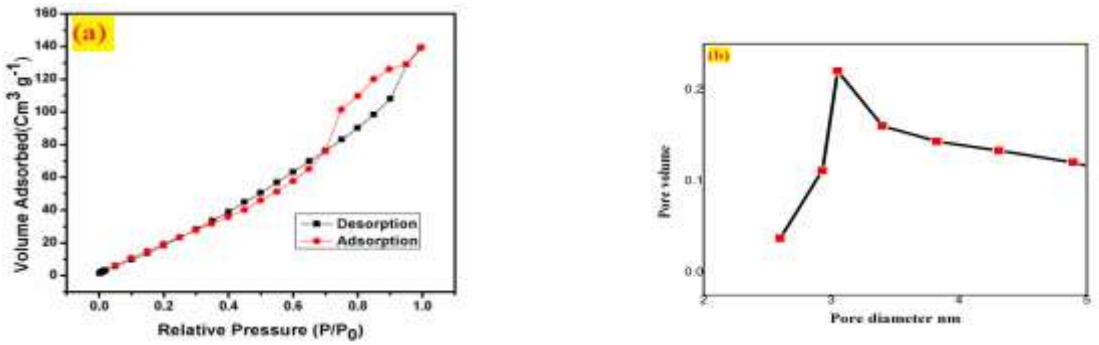


**Fig.8(a)** $N_2$ adsorption-desorption isotherms of $Ni_{0.5}Mg_{0.5}Fe_2O_4$with
**(b)** Pore size distribution plot

### 3.9 Cyclic voltammetry

By utilizing the formula, it is able to calculate the specific capacitance (Cs) of the nickel magnesium ferrite $Ni_{1-x}Mg_xFe_2O_4$ (x=0.5) electrode.

$$Cs = \frac{Q}{\Delta v.m}$$

Where Cs represents the specific capacitance measured in Farads per gram ($Fg^{-1}$), Q is the charge passed during cyclic voltammetry measurement in Coulombs (C), Δv is the potential scan range in volts (V), and m is the mass of the active material on the electrode in grams (g). To calculate the specific capacitance, the values of Q, Δv, and m need to be known for each scan rate (2 $mVs^{-1}$, 5 $mVs^{-1}$, and 10 $mVs^{-1}$) at which the cyclic voltammetry measurements were conducted. In this study, the specific capacitance (Cs) of the $Ni_{0.5}Mg_{0.5}Fe_2O_4$ electrode was determined using electrochemical analysis with a fixed scan rate ranging from 2 to 10 $mVs^{-1}$. The experimental setup was a three-electrode setup with the platinum wire serving as the counter electrode, the sample serving as the working electrode, and Ag/AgCl serving as the reference electrode. A 0.2 M tetra butyl ammonium perchlorate electrolyte was used.

A potential range of -1.5 to 2 V was used for the cyclic voltammetry observations. Fig.9 displays the cyclic voltammograms of $Ni_{1-x}Mg_xFe_2O_4$ (x=0.5) electrodes at scan rates of 2 $mVs^{-1}$ 5 $mVs^{-1}$, and 10 $mVs^{-1}$. The outcomes designated that the specific capacitance values decreased with higher scan rates. This can be attributed to the limited time available for the diffusion and movement of electrolytic ions, which directly affects their accessibility to certain active surface areas of the electrodes.

Precisely, the $Ni_{1-x}Mg_xFe_2O_4$ (x=0.5) electrode exhibited the highest specific capacitance of 412 $Fg^{-1}$ at the lowermost scan rate of 2 $mVs^{-1}$. However, at a higher scan rate of 10 $mVs^{-1}$, the specific capacitance decreased to 68 $Fg^{-1}$. Comparing these results to a previously reported work by Wongpratat *et al;* [29]. It was found that on a scan rate of 2 $mVs^{-1}$, the reported specific capacitance for $Ni_{0.5}Mg_{0.5}Fe_2O_4$ was 82 $Fg^{-1}$, which is lower than the specific capacitance value obtained in this study. Similarly, on a scan rate of 10 $mVs^{-1}$, the reported specific capacitance was 48 $Fg^{-1}$, consistent with the findings of this investigation. The enhanced crystallinity of the $Ni_{0.5}Mg_{0.5}Fe_2O_4$ nanoparticles was confirmed by the higher specific capacitance value detected in this investigation.

Additionally, the specific capacitance of $MgFe_2O_4$ reported in another work was 178.34 $Fg^{-1}$ at a scan rate of 2 $mVs^{-1}$[29], while $NiFe_2O_4$ nanoparticles presented a specific capacitance of 127 $Fg^{-1}$ at a lowermost scan rate [30]. These values provide a reference for the specific capacitance of $MgFe_2O_4$ and $NiFe_2O_4$ nanoparticles in different experimental conditions. The enhanced crystallinity of the $Ni_{0.5}Mg_{0.5}Fe_2O_4$ nanoparticles observed in this present investigation could be one of the reasons for the higher specific capacitance values obtained compared to the previous work by Wongpratat *et al.;* [29].

Overall, this work demonstrates that the substitution of Magnesium in Nickel spinel ferrites ($Ni_{1-x}Mg_xFe_2O_4$) nanoparticles results in improved overall electrochemical performance. The materials' improved electrochemical performances and the results of the XRD, EDX, and XPS investigations all support the idea that this substitution directly influences the materials' electrochemical properties.

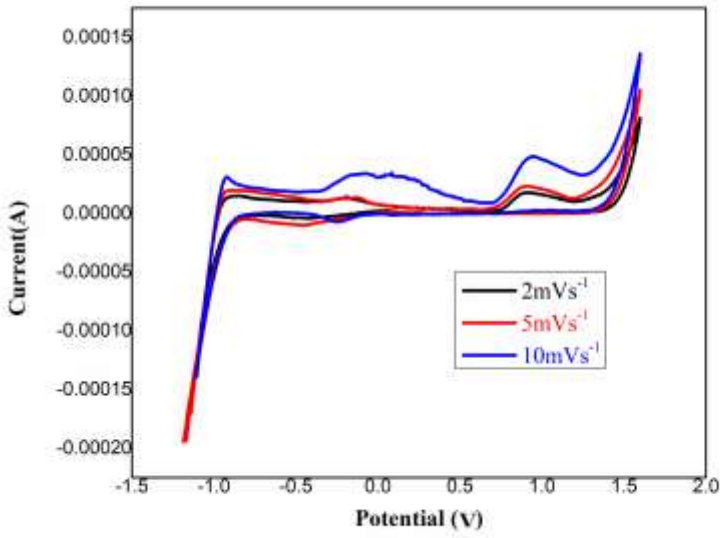


**Fig.9.** CV curves of the sample $Ni_{1-x}Mg_xFe_2O_4$ (x=0.5) at the scan rate of $2mVs^{-1}$, $5mVs^{-1}$, $10mVs^{-1}$

**Table.4** Specific Capacitance value of $Ni_{0.5}Mg_{0.5}Fe_2O_4$ (700 ºC) for different scan rates

| Scan rate ($mVs^{-1}$) | Specific capacitance ($Fg^{-1}$) |
|---|---|
| 2 | 412 |
| 5 | 326 |
| 10 | 68 |

## CONCLUSION

Magnesium-doped nickel ferrite nanoparticles were created using the co-precipitation technique. Analysis of the X-ray diffraction pattern confirmed the presence of a cubic spinel structure in the nickel ferrite samples doped with magnesium. Scanning electron microscopy and high-resolution transmission electron microscopy investigations, along with selected area electron diffraction patterns, revealed that the synthesized composites exhibited a roughly spherical shape with some agglomeration. Energy dispersive x-ray spectroscopy analysis supported the composition of the sample, confirming the presence of nickel (Ni), magnesium (Mg), iron (Fe), and oxygen (O) elements. Fourier-transform infrared spectroscopy provided further evidence of compound formation. Utilizing cyclic voltammetry techniques, the electrochemical performance of the synthesized nanoparticles was assessed. The $NiMgFe_2O_4$ nanoparticles demonstrated a significantly high specific capacitance value of 412 $Fg^{-1}$ on a scan rate of 2 $mVs^{-1}$, indicating their superior supercapacitive properties. This result highlights the potential of the synthesized nanoparticles for advanced supercapacitor applications, as evidenced by their high specific capacitance value offering improved energy storage capacities.

## REFERENCE

[1] Malima, N.M., Khan, M.D., Choi, J., Gupta, R.K., Mashazi, P., Nyokong, T. and Revaprasadu, N., 2021. Solventless synthesis of nanospinel $Ni_{1-x}Co_xFe_2O_4$ ($0 \leq x \leq 1$) solid solutions for efficient electrochemical water splitting and supercapacitance. *RSC advances*, *11*(49), pp.31002-31014.

[2]Samuel, E., Aldalbahi, A., El-Newehy, M., El-Hamshary, H. and Yoon, S.S., 2021. Nickel ferrite beehive-like nanosheets for binder-free and high-energy-storage supercapacitor electrodes. *Journal of Alloys and Compounds*, *852*, p.156929.
[3] Zhai, Q., Rahardjo, H., Satyanaga, A., Zhu, Y., Dai, G. and Zhao, X., 2021. Estimation of wetting hydraulic conductivity function for unsaturated sandy soil. *Engineering Geology*, *285*, p.106034.
[4] Uma, J., Banumathi, S., Maheswaran, R., Senthilkumar, N. and Balraj, B., 2021. Green synthesis of $ZnMn_2O_4$ nanoparticles for supercapacitor applications. *Journal of Superconductivity and Novel Magnetism*, *34*, pp.817-823.
[5] Soam, A., 2021. Application of ferrites as electrodes for supercapacitor. *Ferrites Synth. Appl.*, *55*, p.99381.
[6] Scindia, S.S., Kamble, R.B. and Kher, J.A., 2019. Nickel ferrite/polypyrrole core-shell composite as an efficient electrode material for high-performance supercapacitors. *AIP Advances*, *9*(5).
[7] Wang, Z., Yang, Y., Olmsted, D.L., Asta, M. and Laird, B.B., 2014. Evaluation of the constant potential method in simulating electric double-layer capacitors. *The Journal of chemical physics*, *141*(18).
[8] Jang, Y., Jo, J., Jang, H., Kim, I., Kang, D. and Kim, K.Y., 2014. Activated carbon/manganese dioxide hybrid electrodes for high performance thin film supercapacitors. *Applied Physics Letters*, *104*(24).
[9] Bell, T.E., Ménard, H., Carballo, J.M.G., Tooze, R. and Torrente-Murciano, L., 2020. Hydrogen production from ammonia decomposition using $Co/\gamma\text{-}Al_2O_3$ catalysts–insights into the effect of synthetic method. *International Journal of Hydrogen Energy*, *45*(51), pp.27210-27220.
[10] Niu, J., Shao, R., Liang, J., Dou, M., Li, Z., Huang, Y. and Wang, F., 2017. Biomass-derived mesopore-dominant porous carbons with large specific surface area and high defect density as high performance electrode materials for Li-ion batteries and supercapacitors. *Nano energy*, *36*, pp.322-330.
[11] Ponnamma, D., Aljarod, O., Parangusan, H. and Al-Maadeed, M.A.A., 2020. Electrospun nanofibers of PVDF-HFP composites containing magnetic nickel ferrite for energy harvesting application. *Materials Chemistry and Physics*, *239*, p.122257.
[12] Malarvizhi, M., Meyvel, S., Sandhiya, M., Sathish, M., Dakshana, M., Sathya, P., Thillaikkarasi, D. and Karthikeyan, S., 2021. Design and fabrication of cobalt and nickel ferrites based flexible electrodes for high-performance energy storage applications. *Inorganic Chemistry Communications*, *123*, p.108344.
[13] Ruscic, B., Pinzon, R.E., Von Laszewski, G., Kodeboyina, D., Burcat, A., Leahy, D., Montoy, D. and Wagner, A.F., 2005. Active Thermochemical Tables: thermochemistry for the 21st century. In Journal of Physics: Conference Series (Vol. 16, No. 1, p. 561). IOP Publishing.
[14] Raza, W., Nabi, G., Shahzad, A., Malik, N. and Raza, N., 2021. Electrochemical performance of lanthanum cerium ferrite nanoparticles for supercapacitor applications. Journal of Materials Science: Materials in Electronics, 32, pp.7443-7454.

[15] Ajeesha, T., Ashwini, A., George, M., Manikandan, A., Mary, J.A., Slimani, Y., Almessiere, M.A. and Baykal, A., 2021. Nickel substituted $MgFe_2O_4$ nanoparticles via co-precipitation method for photocatalytic applications. Physica B: Condensed Matter, 606, p.412660.
[16] Bhandare, S.V., Kumar, R., Anupama, A.V., Mishra, M., Kumar, R.V., Jali, V.M. and Sahoo, B., 2020. Effect of Mg-substitution in Co–Ni-Ferrites: Cation distribution and magnetic properties. Materials Chemistry and Physics, 251, p.123081.
[17] Shweta, G.M., Naik, L.R., Pujar, R.B. and Mathad, S.N., 2021. Influence of magnesium doping on structural and elastic parameters of Nickel Zinc nanoferrites. Materials Chemistry and Physics, 257, p.123825.
[18] Sendhilnathan, S., 2017. Enhancement in dielectric and magnetic properties of $Mg^{2+}$ substituted highly porous super paramagnetic nickel ferrite nanoparticles with Williamson-Hall plots mechanistic view. Ceramics International, *43*(17), pp.15447-15453.
[19] Mund, H.S. and Ahuja, B.L., 2017. Structural and magnetic properties of Mg doped cobalt ferrite nano particles prepared by sol-gel method. Materials Research Bulletin, 85, pp.228-233.
[20] Jesus Mercy, S., Parajuli, D., Murali, N., Ramakrishna, A., Ramakrishna, Y., Veeraiah, V. and Samatha, K., 2021. Correction to: Microstructural, thermal, electrical and magnetic analysis of $Mg^{2+}$ substituted Cobalt ferrite. Applied Physics A, 127, pp.1-1.
[21] Lohar, K.S., Patange, S.M., Shirsath, S.E. and Jadhav, S.S., 2011, December. Structural and frequency dependence dielectric properties of magnesium doped nickel ferrite. In 2011 International Conference on Nanoscience, Technology and Societal Implications (pp. 1-2). IEEE.
[22] Phadatare, M.R., Salunkhe, A.B., Khot, V.M., Sathish, C.I., Dhawale, D.S. and Pawar, S.H., 2013. Thermodynamic, structural and magnetic studies of $NiFe_2O_4$ nanoparticles prepared by combustion method: Effect of fuel. Journal of Alloys and Compounds, 546, pp.314-319.
[23] Ilhan, S., Izotova, S.G. and Komlev, A.A., 2015. Synthesis and characterization of $MgFe_2O_4$ nanoparticles prepared by hydrothermal decomposition of co-precipitated magnesium and iron hydroxides. Ceramics International, 41(1), pp.577-585.
[24] Lei, Y., Mao, L., Zhu, H. and Yao, J., 2021. Development of catechol- functionalized chitosan/poly (vinyl alcohol) nanocomposite films incorporated with dual network coated layered clay for active packaging applications. Journal of Applied Polymer Science, 138(42), p.51251.
[25] El-Genk, M.S. and Tournier, J.M., 2005. A review of refractory metal alloys and mechanically alloyed-oxide dispersion strengthened steels for space nuclear power systems. *Journal of Nuclear Materials*, 340(1), pp.93-112.
[26] Dojcinovic, M.P., Vasiljevic, Z.Z., Rakocevic, L., Pavlovic, V.P., Ammar-Merah, S., Vujancevic, J.D. and Nikolic, M.V., 2023. Humidity and Temperature Sensing of Mixed Nickel–Magnesium Spinel Ferrites. Chemosensors, 11(1), p.34.
[27] Revathi, R., Sukumar, M., Kumar, A., Gupta, M., Udhaya, P.A., Sehgal, S.S., Pandit, B., Sundararajan, M., Subramani, A., Dash, C.S. and Senthilkumar, N., 2023. Facile Synthesis of $Ni^{2+}$

Doped $MgFe_2O_4$ Spinel Nanoparticles: Structural, Optical, Magnetic, and Dielectric Behavior. *Journal of Inorganic and Organometallic Polymers and Materials*, pp.1-13.

[28] Šutka, A., Pärna, R., Käämbre, T. and Kisand, V., 2015. Synthesis of p-type and n-type nickel ferrites and associated electrical properties. Physica B: Condensed Matter, 456, pp.232-236.

[29] Wongpratat, U., Tipsawat, P., Khajonrit, J., Swatsitang, E. and Maensiri, S., 2020. Effects of nickel and magnesium on electrochemical performances of partial substitution in spinel ferrite. Journal of Alloys and Compounds, 831, p.154718.

[30] Sen, P. and De, A., 2010. Electrochemical performances of poly (3, 4-ethylenedioxythiophene)–$NiFe_2O_4$ nanocomposite as electrode for supercapacitor. Electrochimica Acta, 55(16), pp.4677-4684.

[31] Moradmard, H., Shayesteh, S.F., Tohidi, P., Abbas, Z. and Khaleghi, M., 2015. Structural, magnetic and dielectric properties of magnesium doped nickel ferrite nanoparticles. Journal of Alloys and Compounds, 650, pp.116-122.

[32] Sivakumar, P., Ramesh, R., Ramanand, A., Ponnusamy, S. and Muthamizhchelvan, C., 2011. Synthesis and characterization of nickel ferrite magnetic nanoparticles. Materials Research Bulletin, 46(12), pp.2208-2211.

[33] Jeseentharani, V., George, M., Jeyaraj, B., Dayalan, A. and Nagaraja, K.S., 2013. Synthesis of metal ferrite (MFe2O4, M= Co, Cu, Mg, Ni, Zn) nanoparticles as humidity sensor materials. *Journal of experimental nanoscience*, *8*(3), pp.358-370.

[34] Al-Senani, G.M., Al-Fawzan, F.F., Almufarij, R.S., Abd-Elkader, O.H. and Deraz, N.M., 2022. Biosynthesis, Physicochemical and Magnetic Properties of Inverse Spinel Nickel Ferrite System. *Crystals*, *12*(11), p.1542.